Multiscale photonic imaging of the native and implanted cochlea

Daniel Keppeler[a,b], Christoph A. Kampshoff[a,b,c], Anupriya Thirumalai[a,b], Carlos J. Duque-Afonso[a,b], Jannis J. Schaeper[d], Tabea Quilitz[a,b], Mareike Töpperwien[d], Christian Vogl[a,b], Roland Hessler[e], Alexander Meyer[b,c], Tim Salditt[d,f], and Tobias Moser[a,b,c,f,g,1]

[a]Institute for Auditory Neuroscience, University Medical Center Göttingen, 37075 Göttingen, Germany; [b]InnerEarLab, University Medical Center Göttingen, 37075 Göttingen, Germany; [c]Department of Otolaryngology, University Medical Center Göttingen, 37075 Göttingen, Germany [d]Institute for X-ray Physics, University of Göttingen, 37075 Göttingen, Germany; [e]MED-EL, 6020 Innsbruck, Austria; [f]Cluster of Excellence "Multiscale Bioimaging: From Molecular Machines to Networks of Excitable Cells," University of Göttingen, 37075 Göttingen, Germany; and [g]Auditory Neuroscience and Optogenetics Laboratory, German Primate Center, 37075 Göttingen, Germany

The cochlea of our auditory system is an intricate structure deeply embedded in the temporal bone. Compared with other sensory organs such as the eye, the cochlea has remained poorly accessible for investigation, for example, by imaging. This limitation also concerns the further development of technology for restoring hearing in the case of cochlear dysfunction, which requires quantitative information on spatial dimensions and the sensorineural status of the cochlea. Here, we employed X-ray phase-contrast tomography and light-sheet fluorescence microscopy and their combination for multiscale and multimodal imaging of cochlear morphology in species that serve as established animal models for auditory research. We provide a systematic reference for morphological parameters relevant for cochlear implant development for rodent and nonhuman primate models. We simulate the spread of light from the emitters of the optical implants within the reconstructed nonhuman primate cochlea, which indicates a spatially narrow optogenetic excitation of spiral ganglion neurons.

light-sheet fluorescence microscopy | X-ray phase-contrast tomography | cochlear implant | optogenetics | hearing restoration

In the case of profound sensorineural hearing impairment, cochlear implants (CIs) partially restore hearing by providing auditory information to the brain via electrical stimulation of the spiral ganglion neurons (SGNs). CIs enable speech understanding in the majority of the ~700,000 users worldwide. However, current clinical CIs are limited by their wide current spread (1) resulting in poor coding of spectral information (2). Recently, cochlear optogenetics was proposed for stimulating the auditory nerve by light (3–10). As light can be better confined in space, the spread of excitation in the cochlea is lower (3, 9–11) and, hence, future optical CIs (oCIs) promise improved speech comprehension—especially in noisy background—as well as greater music appreciation.

For the technical development of oCIs toward a future medical device, major efforts are currently being undertaken to devise multichannel optical stimulators for the cochlea (10, 12–17). As is the case for the electrodes of current CIs, future oCIs will place multiple stimulation channels, here microscale emitters, along the tonotopic axis of the cochlea. Further development of the oCIs requires precise estimates of parameters such as scala tympani size, optimal probe stiffness, and bending radius. Moreover, cochlear optogenetics employs gene transfer to the SGNs for which adeno-associated viruses (AAVs) seem promising candidate vectors (3–5, 8). AAV delivery has used injection of virus suspension via the round window (4, 8) or directly into Rosenthal's canal (5, 9, 10). Therefore, the volumes of Rosenthal's canal and the scalae tympani, vestibuli and media needed to be evaluated in order to estimate the required virus load for injection. Finally, the sensorineural status of the cochlea is highly relevant for future gene therapy and CI stimulation, and hence, quantitative imaging of sensory cells and neurons is an important objective.

Here, we employed multiscale X-ray phase-contrast tomography (XPCT) and light-sheet fluorescence microscopy (LSFM) and provide an analysis of cochlear morphology for mice, rats, gerbils, guinea pigs, and marmosets. Each of these animal models offers unique advantages for auditory research. The mouse is readily available for genetic manipulation (e.g., ref. 18). Channelrhodopsin-expressing transgenic lines are available also for rats (19, 20) that offer a larger cochlea and can carry heavier implants than mice (21–24). Similarly, gerbils and guinea pigs are established rodent models for auditory research with larger-sized cochleae. Moreover, gerbils, which have low-frequency hearing more similar to humans, have already been employed for cochlear optogenetics (5, 9, 10, 24). Finally, we analyzed the cochlea of the common marmoset, as an established nonhuman primate model for auditory research (e.g., refs. 25, 26). Marmosets possess a rich vocalization repertoire and share a pitch perception mechanism with humans (27). Therefore, we compared cochlear insertion of newly designed oCIs with electrical cochlear implants (eCI) and modeled the optical spread of excitation in the marmoset cochlea.

Results

Multiscale, Multimodal Photonic Imaging of Cochlear Morphology. We have used XPCT and LSFM for multiscale, multimodal photonic imaging of cochlear morphology. High resolution X-ray

---

Significance

For the development of gene therapy and optical cochlear implants (oCI), detailed knowledge of the cochlear morphology is crucial. Here, we employed multiscale X-ray and fluorescence imaging for quantitative assessment of scala tympani, vestibuli, and media, as well as the spiral ganglion in Rosenthal's canal for various species commonly used in auditory research. Furthermore, we demonstrate the feasibility of oCI implantation for rodents and marmosets, as a nonhuman primate model. Using modeling of light propagation from the emitters of the oCI, we estimate the frequency selectivity and range covered by optical stimulation within the cochlea.

NEUROSCIENCE

www.manaraa.com

tomography for three-dimensional (3D) histology and micro-anatomy can either be achieved by labeling with radiocontrast agents (28, 29) or by propagation-based phase contrast (30–34). Phase-sensitive image formation requires partial coherence and was therefore largely dependent on synchrotron radiation. With the advent of higher brightness sources and small spot sizes, however, propagation-based XPCT can now also be implemented at compact, in-house X-ray instrumentation (35, 36). Here, this has enabled us to resolve cochlear soft tissue (Fig. 1*A*), where we focused on the spiral ganglion and the basilar membrane (Fig. 1 *B* and *C*). Our custom XPCT setup allowed a multiscale study of the cochlear anatomy down to a voxel size of 2 µm. An example of a raw volume rendering of a guinea-pig cochlea dataset is shown in Fig. 1*C*. The hemisected cochlear reconstruction reveals scala tympani and the combined scalae vestibuli and media, separated by the basilar membrane as well as Rosenthal's canal. The same setup enables the analysis of differently sized cochleae from various species: from mice to marmosets (Fig. 1*D*) (37). The species differences in shape, number of turns, overall size of the cochlea, and position of the round and oval windows can be appreciated in Fig. 1*D*. Human data were reconstructed from published micro-computed tomography data (38). The quantification of the cochlear morphology as required, for example, for the design of appropriately shaped and sized o/eCIs as well as for modeling of optical SGN stimulation by oCI is presented below.

While XPCT provides access to morphology of the fixed, but otherwise untreated, cochlea, it does not provide molecular information. Therefore, we turned to LSFM of decalcified, cleared, and immunostained cochleae as a complementary multiscale imaging modality (Fig. 2*A*). We adapted the iDisco+ protocol (39) to the cochlea ("cDisco," *SI Appendix*, Figs. S1 and S2). Following decalcification, cDisco with dibenzyl ether for refractive index matching enabled good LSFM imaging of parvalbumin-immunolabeled SGNs and hair cell results for the cochleae of mice (Fig. 2*D* and *SI Appendix*, Fig. S3), gerbils (not shown), and marmosets (Fig. 2*D*). We note that protocols using other refractive index-matching compounds such as methyl salicylate benzyl benzoate were not permissive for our study as this could have inflicted damage to our microscope (UltraMicroscope II, LaVision Biotech).

As expected for the species-dependent volume of the bone, the time required for decalcification, clearing, and immunostaining ranged from ∼5 wk for the mouse to, on average, 20 wk for marmoset cochleae. LSFM allowed 3D imaging of the organ of Corti as well as of the spiral ganglion, resolving hair cells and SGNs across all cochlear turns (Fig. 2 *A–C*). This was used to estimate the length of the organ of Corti and the tonotopic map (40) of the mouse and marmoset cochlea (Fig. 2 *D* and *E*). Moreover, LSFM of immunolabeled hair cells and SGNs promises quantitative information about the sensorineural status and the expression of transgenes following gene therapy of the cochlea. In a first effort toward quantitative cellular analysis, we counted SGNs in LSFM datasets of the mouse cochlea. Following manual generation of a mask of Rosenthal's canal, we used automated segmentation of SGN somata by the blob-finder feature of arivis Vision4D software (Fig. 2*G* and *SI Appendix*, Fig. S3). The blob-finder builds on detection of round objects of a predefined range of diameters and above a certain fluorescence threshold, which is followed by a watershed algorithm to further split objects. The outcome of the segmentation depends on the quality of the immunostaining and imaging (*SI Appendix*, Figs. S3 and S4): for three LSFM datasets of cochleae with permissive quality, we found on average 9,106 ± 724 SGNs, which agrees well with previously reported SGN counts for the mouse cochlea [7,920 ± 4,230 (41)].

Finally, we performed sequential multimodal imaging, where LSFM of the cleared and immunostained marmoset cochlea was followed by highly resolved synchrotron XPCT (Fig. 3). The cleared cochlea was mounted in a falcon tube filled with dibenzyl ether and provided excellent phase contrast. Overview scans of the whole cochlea using a widened beam (after focusing by Kirkpatrick–Baez mirrors) were acquired at a voxel size of 3.05 µm (Fig. 3 *A* and *C*) and overlaid onto the corresponding LSFM images (Fig. 3*D*). Region-of-interest scans were performed using a parallel beam at a voxel size of 650 nm (Fig. 3 *B* and *E–F*). Parallel-beam imaging enabled resolving individual SGNs (Fig. 3*E*). Following manual generation of a mask of Rosenthal's canal, we used automated segmentation of SGN somata by the blob-finder feature of arivis Vision4D software (Fig. 3 *F* and *H*). Based on the high electron density of SGN nuclei (e.g., Fig. 3*F*), automated cell counting was feasible without labeling or clearing (uncleared cochlea, reference *SI Appendix*, Fig. S5). In addition to cell counting, quantitative morphological parameters such as nuclear sphericity or volume can also be extracted automatically for each object. All segmented objects can be plotted in higher-dimensional histograms to quantify the distribution of morphological parameters (*SI Appendix*, Fig. S5).

Quantifying Cochlear Morphology for Preclinical Studies on Drug Administration and Cochlear Implantation. Preclinical studies on intracochlear drug/virus administration, CI design, and implantation as well as modeling of SGN stimulation require reliable data on cochlear morphology for the animal models of interest such as rodents and nonhuman primates in relation to humans. For defining injection volumes and modeling pharmacodynamics, volume measurements (42) are highly relevant. Table 1 provides our X-ray-imaging–based volume estimates for scala tympani, the combined scalae vestibuli and media as well as Rosenthal's canal for mouse, rat, gerbil, guinea pig, marmoset, and human, and a comparison with literature values is presented for mouse and guinea pig in *SI Appendix*, Table S1.

Preclinical CI studies require estimates of scala tympani morphology and basilar membrane length. We measured basilar membrane length by X-ray imaging, which in mice was about a fifth of the human, while it was approximately half the human length in guinea pigs and marmosets (Table 1). The X-ray data were comparable to estimates based on LSFM of inner hair cells (IHCs) in the organ of Corti of mice and marmosets (Table 1). Next, we quantified scala tympani morphology from 3D reconstruction of X-ray tomography data (Fig. 1). We calculated the centroid for virtual sections of scala tympani along the turns by determining the minimum radius by means of the closest point on the cavity's surface for each sampling point (Fig. 4*A*). This resulted in a 3D centerline for scala tympani (Fig. 4*A*). For all analyzed species, the minimum radius was largest at the cochlear base close to the round window and smallest at the apex (Fig. 4*B*). Assuming a CI covers 60% of scala tympani length (43), the tip of the CI should be limited to a radius of 0.13/0.12/0.12/0.15/0.23/0.44 mm in mice, rats, gerbils, guinea pigs, marmosets, and humans, respectively (Fig. 4*B*). Cross-sectional area and perimeter of scala tympani of the species of interest are displayed in *SI Appendix*, Fig. S6.

The bending radius, here referred to as radius of curvature (short curvature), has great relevance for the design of waveguide-based and light-emitting diode (LED) oCIs. Cladding and core of waveguides need to comply with the bending radius to ensure mechanical integrity and total internal reflection, while minimizing scattering losses at their interface. LEDs such as blue GaN-LEDs (44) are stiff, and hence, their size and pitch within the array on a flexible substrate (13) need to accommodate the curvature of the coiled scala tympani. To be able to cover 60% of the cochlear length in mice, a radius of curvature of 0.29 mm has to be obeyed. In contrast, the cochleae of rats, marmosets, or humans provide greater radii of curvature: 0.51 mm, 0.80 mm, and 1.64 mm. Regardless, all radii of curvature require the use of microscale emitters such as µLEDs for the manufacturing of optoelectronic (active) oCIs. Considering such µLED-based oCIs that feature a mostly two-dimensional shape due to their circuit plane, an oval-shaped design
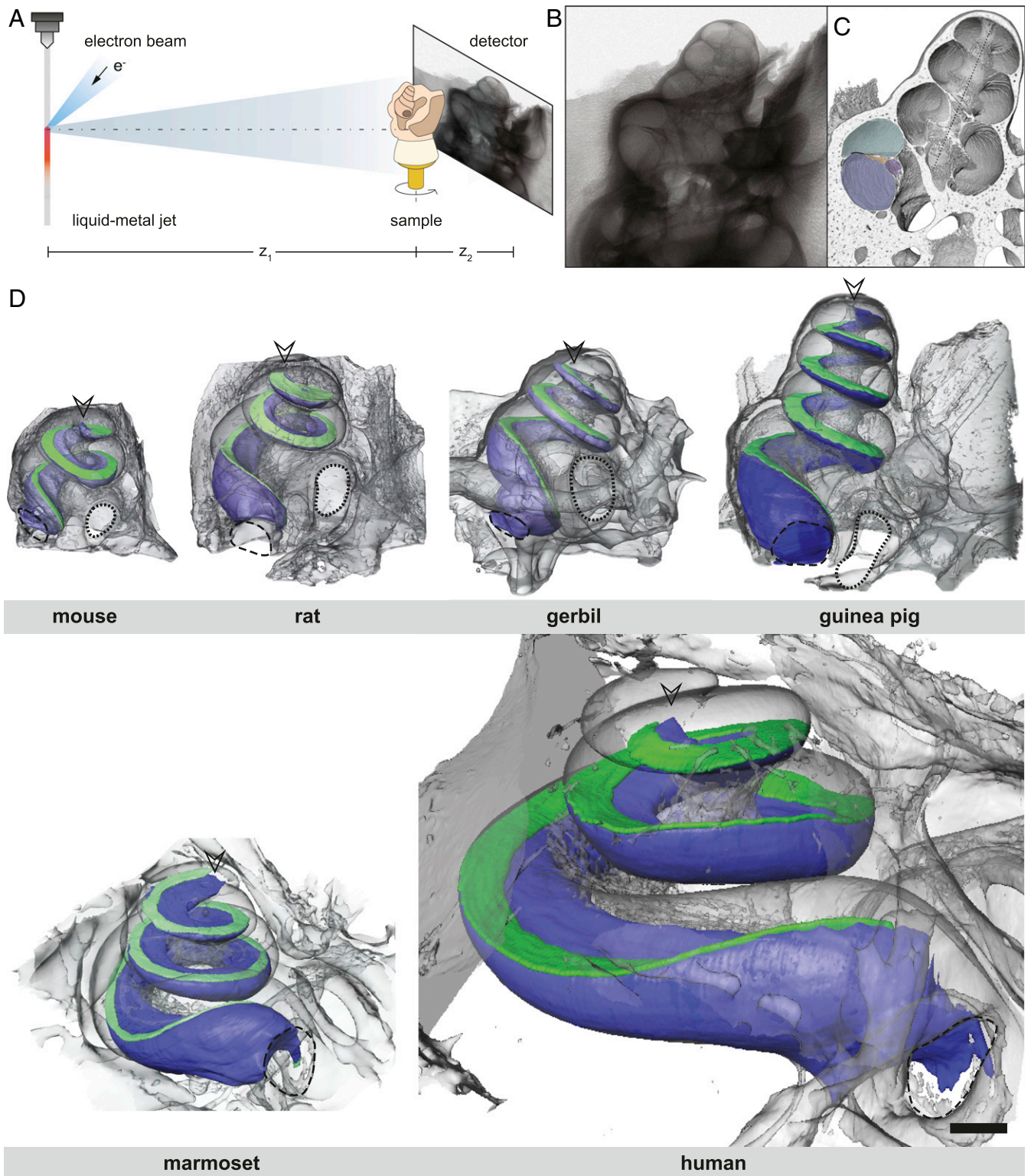
Fig. 1. X-ray tomography-based 3D models of rodent and primate cochleae. (*A*) In-house experimental setup. X-rays are generated by a liquid-metal jet microfocus tube. Based on optimized geometric parameters and detection by high-resolution scintillator-based charge-coupled device (CCD) camera, phase and absorption contrast can be exploited for image formation. (*B*) Raw two-dimensional projection showing edge enhancement indicative of phase-sensitive image formation by propagation. The projections are then fed into the phase retrieval algorithm, followed by tomographic reconstruction. (*C*) Volume rendering of reconstructed image stack. Scala tympani (blue), scala vestibuli and media (green, combined as Reissners' membrane could not be reliably detected), Rosenthal's canal (purple), osseous spiral lamina (orange), basilar membrane (black line), and modiolar axis (dashed line). (*D*) Segmented cochleae visualized with bone (gray), basilar membrane (green), scala tympani (blue), round window (dashed line), oval window (dotted line), and apex (arrowhead). Datasets are available under ref. 37. (Scale bar, 1 mm.)
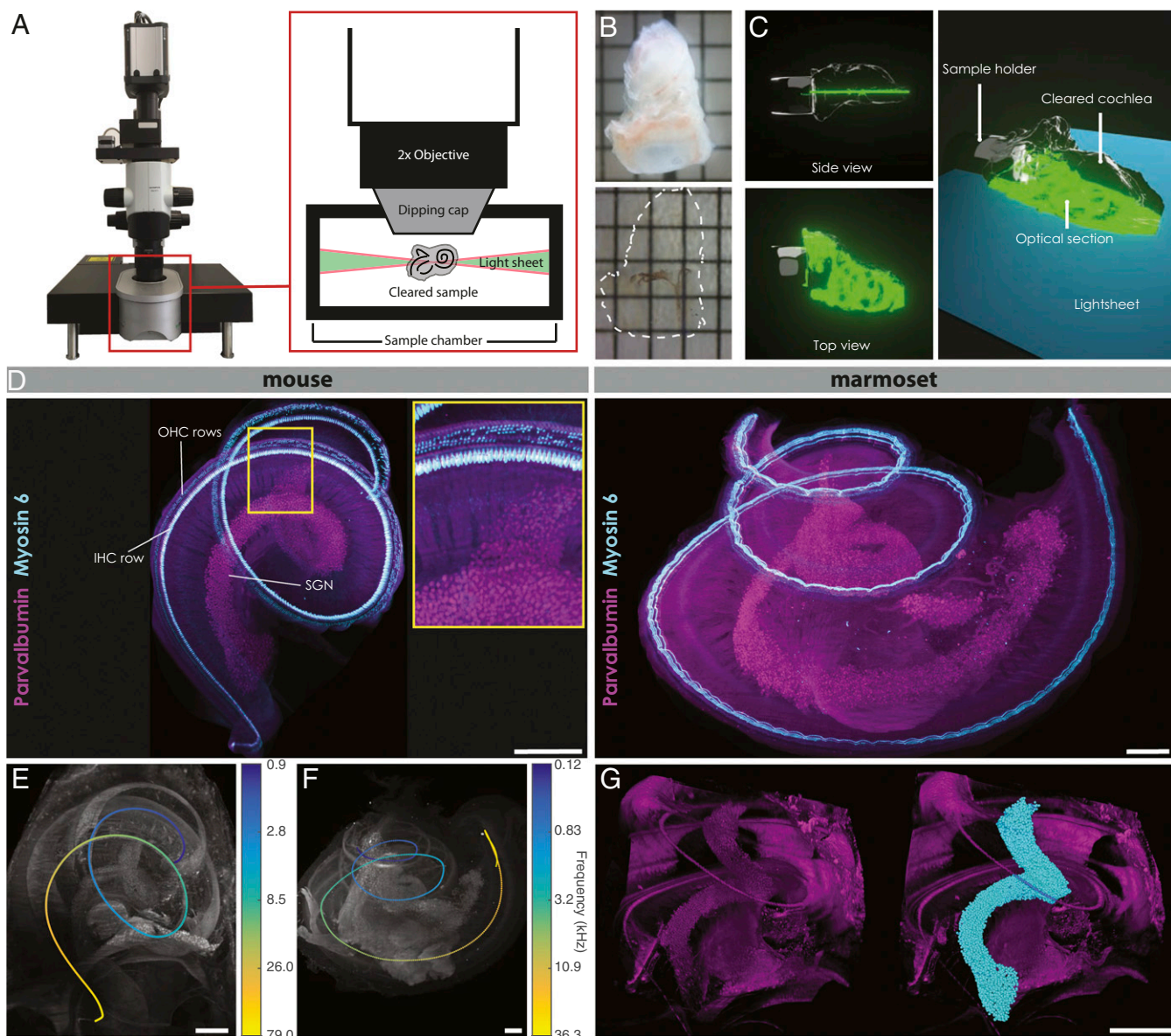
Fig. 2. Molecular imaging of the cleared mouse and marmoset cochlea by light-sheet fluorescence microscopy. (*A*) Light-sheet fluorescence microscope (UltraMicroscope II, LaVision Biotech) with a schematic representation of its sample chamber. The laser beam is formed into a light sheet by two cylindrical lenses and illuminates the whole sample in one level. The 2× objective is protected against the clearing medium by a dipping cap. The sample is moved through the light sheet, and a scientific Complementary metal-oxide-semiconductor (sCMOS) detector is detecting every illuminated level. (*B*) Cochlea clearing using the modified iDisco+ protocol (39). To enable the light sheet to penetrate the whole sample, the cochlea has to be cleared. The upper image shows a native mouse cochlea in phosphate-buffered saline (PBS) (one square = 1 mm), the lower image shows the same mouse cochlea cleared in dibenzyl ether (DBE), an organic compound with a refractive index of 1.562. (*C*) Schematic representation of LSFM imaging. Side view, top view, and high-angle view. (*D*) LSFM image of a mouse cochlea (*Left*) and a marmoset cochlea (*Right*); the bone was cropped manually for better illustration, immunostaining with anti-parvalbumin (magenta) to stain the SGNs and anti-myosin 6 (cyan) to stain IHCs and outer hair cells (OHCs), the yellow square shows a zoom (282 μm × 374 μm) in the medial turn region. (Scale bar, 300 μm.) (*E*) The tonotopic axis along the IHC row is shown as color-coded spline in the mouse cochlea. The frequency (in kHz) was calculated with the Greenwood function. Immunostaining with anti-parvalbumin (gray). (Scale bar, 300 μm.) (*F*) The tonotopic axis along the IHC row shown as color-coded spline in the marmoset cochlea. The frequency (in kHz) was calculated with the Greenwood function. Immunostaining with anti-parvalbumin (gray). (Scale bar, 300 μm.) (*G*) Uncropped LSFM image of a left-ear mouse cochlea (*Left*) and automatically segmented SGNs (cyan, *Right*). Immunostaining with anti-parvalbumin (magenta) with a count of 9,402 cells (see also *SI Appendix*, Fig. S3) and an F1 score of 97% for the detection error estimation (details in *SI Appendix*, Fig. S4). Datasets are available under ref. 37. (Scale bar, 300 μm.)

of the oCI could make use of the about 1.9 times larger width compared with the height of the tympanic duct.

Implantation Studies for oCI and eCI in Different Species. When starting experimental cochlear implantation of oCIs, we first tested various combinations of carrier materials and encapsulations in explanted mouse cochleae. Among the first attempts of oCI insertion, we used

a plain polyimide substrate of 15 μm thickness without encapsulation. It could be implanted into the explanted mouse cochlea up to its full length of 5 mm, but in subsequent X-ray tomography it was found cutting through the basilar membrane ("scala crossing," *SI Appendix*, Fig. S7). Encapsulation of the probes using various approaches was employed to avoid scala crossing. We first turned to dipping into silicone and thereafter spinning the probes,
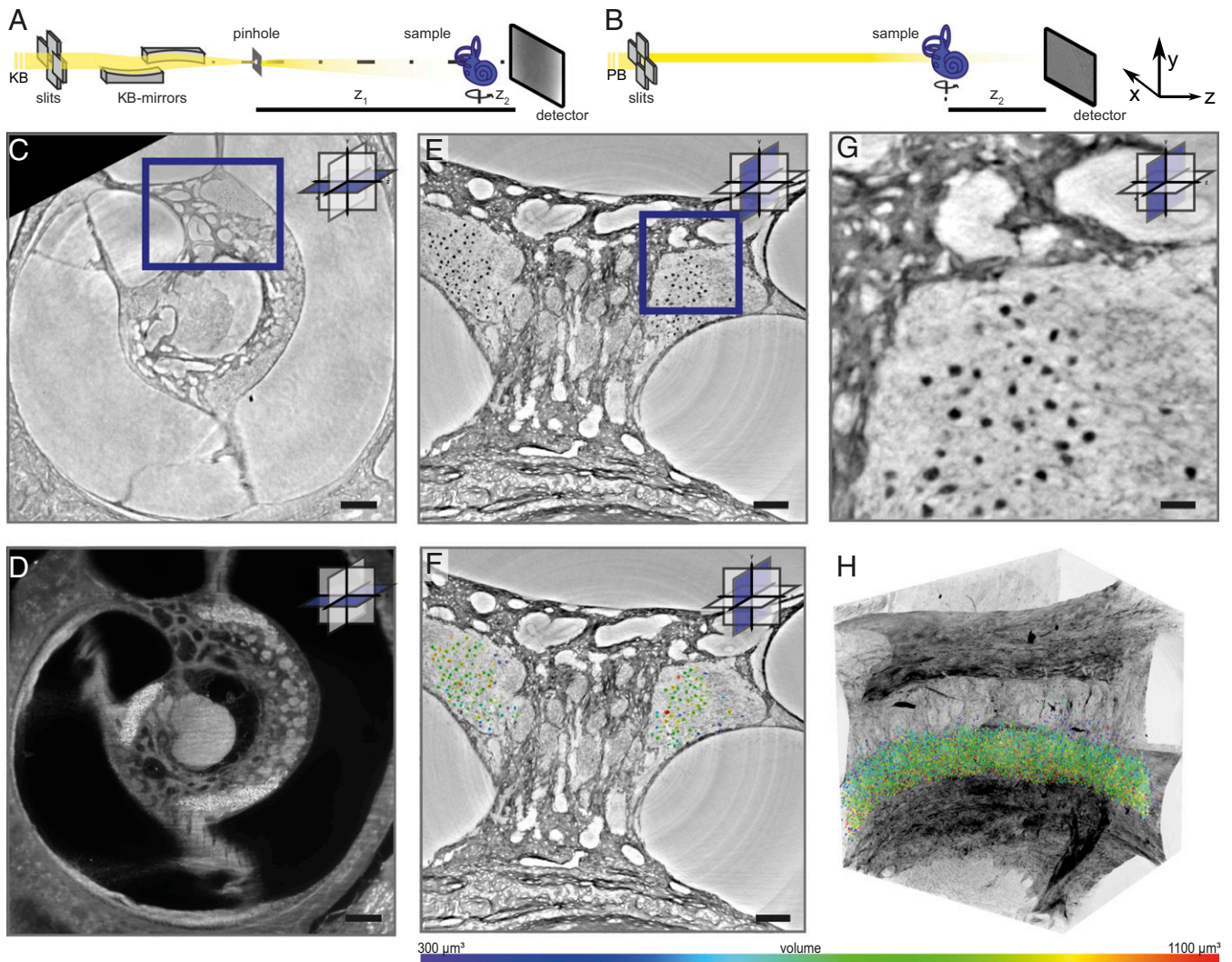
Fig. 3. Sequential imaging of the marmoset cochlea by LSFM and X-ray tomography. (*A* and *B*) Experimental setup for multiscale phase-contrast tomography of Göttingen instrument for nano-imaging with X-rays (GINIX) endstation (P10/PETRAIII) at Deutsches Elektronen Synchrotron (DESY), combining (*A*) overview scans of the entire cochlea in a widened beam (KB: Kirkpatrick–Baez focusing) with field of view (FOV) of 8 × 7 mm at a voxel size of 3.05 μm, and (*B*) parallel beam tomography with FOV of 1.6 × 1.4 mm at a voxel size of 650 nm. (*C–F*) Pictograms indicate coarse orientation of orthogonal slices. (*C*) Virtual slice through the reconstruction volume of the whole cochlea (cleared) with KB setup. (Scale bar, 250 μm.) (*D*) LSFM reconstruction of the same section as in *C* obtained by manual image registration. The cleared cochlea was stained with anti–Tubulin-β 3 (TUBB3) antibody. (Scale bar, 250 μm.) (*E*) Region-of-interest volume scan with parallel beam setup resolves individual SGNs. Region of interest is indicated by a blue rectangle in *C*. (Scale bar, 100 μm.) (*F*) Same region of interest as in *E* with segmented SGNs indicated as circles and colored by volume. (Scale bar, 100 μm.) (*G*) Further zoom into *E* demonstrating image quality of the parallel beam (PB) setup. Zoom area is indicated with a blue rectangle in *E*. (Scale bar, 25 μm.) (*H*) Volume rendering of the region-of-interest scan with segmented SGNs color coded by individual volume. Datasets are available under ref. 37.

which resulted in a cylindrical shape of the polyimide-based probes and mechanical properties that were very well suited for implantation (*SI Appendix*, Fig. S8).

We then turned to encapsulating μLED arrays that were fabricated following the design published earlier (13). Those encapsulated μLED arrays could be inserted into scala tympani of the explanted mouse cochlea via the round window for ~4.6 mm without detectable damage. When approximating the frequency-place map of the mouse (45), the insertion covered a frequency range from 2.5 to 72.2 kHz of a total hearing range from 0.6 to 79.3 kHz which corresponds to 4.9 out of 7.0 octaves, so ~70%. The 93 μLEDs accommodated on the 4.6 mm intracochlear portion would correspond to a dense coverage of ~20 channels per octave. Furthermore, μLED orientation appeared optimal: the active μLED surface was facing Rosenthal's canal, which was achieved solely by the experimenter's choice of the orientation of the probe during cochlear implantation.

We next turned to species with larger cochleae for investigating the utility of mold encapsulation. Using a state-of-the-art mold injection process, a low density μLED array (10, 14) was encapsulated yielding an outer diameter of 340 μm. The probe was inserted into scala tympani of a rat cochlea in situ (13 of 16 μLEDs inside the cochlea, pitch of 300 μm) achieving an implantation depth of 3.6 mm (Fig. 5*B*). Despite the round profile orientation of the probe, μLEDs were well positioned in regard to the Rosenthal's canal. However, the insertion depth was much inferior to what we found above in the explanted cochlea of the mouse with probes coated by dipping in silicone and subsequent spinning (Fig. 5*A*).

Finally, we compared the insertion of eCIs and LED-based oCIs in the cochlea of a nonhuman primate model, the common marmoset. Using cadaver skulls, we performed a posterior tympanotomy (comparable to the clinical approach in humans) and inserted the CIs via the round window. The probes were specifically

Keppeler et al.
Multiscale photonic imaging of the native and implanted cochlea

PNAS | 5 of 11
https://doi.org/10.1073/pnas.2014472118

Table 1. Comparison of cochlear measurements across species

Species	Mouse		Rat		Gerbil		Guinea pig		Marmoset		Human	
n_{XPCT}	3		3		3		1		3		1	
n_{LSFM}*	12								5			
Basilar membrane												
Length (mm), XPCT	6.56	0.17	9.82	0.23	13.20	0.64	20.07	—	17.11	0.83	37.33	—
Length (mm), LSFM	5.75	0.21							17.79	0.94		
Scala tympani												
Length (mm)	4.23	0.11	7.12	0.10	9.37	0.69	14.32	—	14.78	0.81	26.38	—
Volume (μL)	0.52	0.03	1.30	0.04	1.81	0.04	5.48	—	4.65	0.47	43.09	—
Mean radius (mm)	0.13	0.00	0.15	0.01	0.16	0.00	0.21	—	0.23	0.00	0.45	—
Scala vestibuli and media												
Length (mm)	6.34	0.37	9.12	0.37	11.18	0.20	18.94	—	16.18	0.51	31.09	—
Volume (μL)	1.10	0.02	3.38	0.26	4.44	0.01	13.01	—	4.99	0.56	45.89	—
Mean radius (mm)	0.17	0.00	0.22	0.01	0.21	0.01	0.31	—	0.23	0.00	0.41	—
Rosenthal's canal												
Length (mm), XPCT	2.46	0.09	4.54	0.13	6.30	0.53	8.85	—	8.45	0.79	15.50	—
Length (mm), LSFM	2.30	0.10										
Volume (μL)	0.06	0.00	0.15	0.00	0.10	0.07	0.37	—	0.18	0.08	3.26	—
Mean radius (mm)	0.06	0.00	0.07	0.01	0.06	0.00	0.07	—	0.07	0.00	0.16	—

Measurements on segmented adult animal cochleae for XPCT and LSFM datasets. Data are displayed as mean with SD. n indicates the sample size for XPCT and LSFM, respectively.
*LSFM mouse datasets include P14 animals. For details, please see ref. 43.

designed to fit the marmoset cochlea: eCIs had a diameter of 300 μm with 10 electrodes and an electrode spacing of 1,000 μm (right eCI in Fig. 5D) and 1,500 μm (left eCI in Fig. 5D), respectively. oCIs were designed to closely resemble the eCIs with 10 LEDs (250 × 200 μm) and an LED spacing of 500 μm. They were dip coated in silicone with a final diameter of ~260 μm. eCI and oCI could be implanted for maximally 8.9/7.6 mm (Fig. 5 C and D) covering 60/51% of the scala tympani, respectively. In the case of the oCI, 10 LEDs were placed on 4.5 mm with a mean distance of 671 ± 93 μm to the centerline of Rosenthal's canal. For eCIs, the six and seven electrode contacts inside scala tympani had a distance of 674 ± 24 μm from the centerline of Rosenthal's canal.

Modeling Optical Stimulation in the Marmoset Cochlea. Finally, we modeled the spread of light from the LEDs of the implanted oCI building on the morphological analysis of a marmoset cochlea (Fig. 6). The length of the oCI covered ~51% of the tonotopic map with the apical most LED (LED1) facing the 3 kHz region of the cochlea (Fig. 6 A and B). We modeled the spread of light using a Monte Carlo ray tracing model (using TracePro software, for details on material properties, reference *SI Appendix*, Table S2, also see ref. 5) with three million rays from each LED (λ = 473 nm, Cree TR2227 LEDs). In order to study the spread of light from each LED with reference to the tonotopic axis of the cochlea, we queried tonotopic places (Fig. 6A) at the level of the peripheral SGN neurites (localized at the edge of the osseous spiral lamina) and in the center Rosenthal's canal (SGN somata). As demonstrated in Fig. 6B, higher and more confined irradiances were obtained at the level of the peripheral processes for the chosen exemplary LEDs 1, 5, and 10, which is expected given their closer proximity to the LEDs. The differences were least pronounced and the irradiance the lowest for the peripheral processes facing the basal-most LED 10. The irradiances achieved at a 10 mW radiant flux from the LED were more homogenous at the level of the SGN somata in Rosenthal's canal (Fig. 6C). The spectral spread of excitation at this radiant flux was measured by evaluating the tonotopic range over which SGNs got excited (radiant flux threshold of 3 mW translating to a threshold of 0.87 mW/mm² for SGN somas and 1.81 mW/mm² for SGN peripheral neurites, Fig. 6C and *SI Appendix*, Table S3). As expected, the spread of excitation was greater for excitation of SGN somata.

Discussion

In this study, we quantified cochlear morphology in commonly used animal models to enable preclinical studies on innovative therapeutic approaches to deafness. We combined two fundamentally distinct photonic techniques for 3D imaging of the cochlea: XPCT and LSFM. Both allowed us to generate 3D models enabling one to view cochlear structures from any angle. Furthermore, virtual cross-sectioning gave valuable insight in cochlear structures and made structural measurements straightforward. Each imaging modality shows strengths and weaknesses (*SI Appendix*, Table S5): XPCT offers the possibility to precisely quantify the dimensions of cochlear compartments without manipulation of the sample, which enables rapid and nondestructive analysis. Moreover, it serves to localize eCI electrodes and oCI emitters within the implanted scala tympani as required for optimizing CIs and their insertion into the cochlea. LSFM, on the other hand, provides histological details and molecular information. This enables identification of cell types, cell counts, and molecular analysis. However, it requires substantial tissue processing to be carried out over a few weeks prior to imaging. The two imaging modalities complement each other very well for translational studies on hearing restoration. Hence, we finally combined them on the same cochlea performing sequential multimodal imaging by LSFM and XPCT and achieved cellular resolution and automated SGN segmentation with both imaging approaches. Our structural analysis has aided the design of oCIs for mice, gerbils, rats, and marmosets. Moreover, it has enabled realistic computational modeling of the light spread from the individual LEDs of the oCI in the marmoset cochlea prior to behavioral and physiological assessment of frequency selectivity of optogenetic stimulation.

Multiscale, Multimodal Imaging of Cochlear Structure. The intricate cochlear morphology has inspired numerous imaging studies involving various modalities such as magnetic resonance, photonic, and electron microscopic imaging. In fact, for some modalities such as LSFM [first described by Siedentopf and Szigmondy (46)], imaging the cochlea was the first biological application

www.manaraa.com
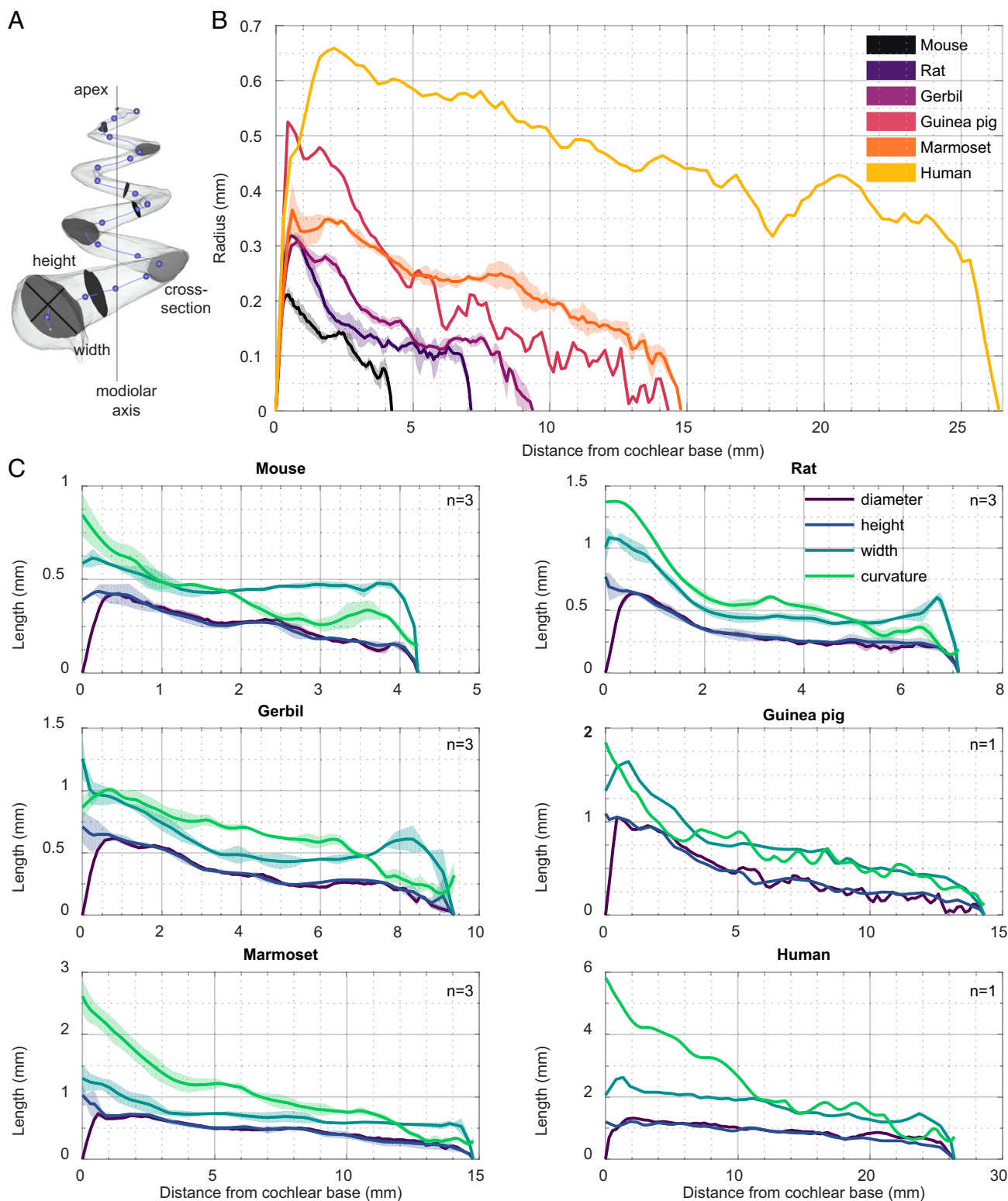
Fig. 4. Measurements of the scala tympani relevant for cochlear implantation. (*A*) Example for a segmented scala tympani (here: guinea pig) with smoothed centerline beginning at the round window (gray dot) derived from X-ray tomography datasets. Centerline was used as trajectory for virtual cross-sections (exemplary cross-sections depicted in gray, every 50th sampling point in blue). Segmented models were derived from X-ray tomography datasets. For further analysis, reference *SI Appendix*, Fig. S6. (*B*) Smallest radius of scala tympani from base to apex. Data were scaled along the distance dimension to fit the mean length of scala tympani. Shaded regions indicate mean ± SD, animal count (*n*) as in *C*. (*C*) Measurements of parameters relevant for CI design considerations. The diameter was derived from the centerline calculation; height and width were determined in virtual sections; curvature represents the radius from the modiolar axis to the centerline of scala tympani. Please note that different species are plotted in different scales.
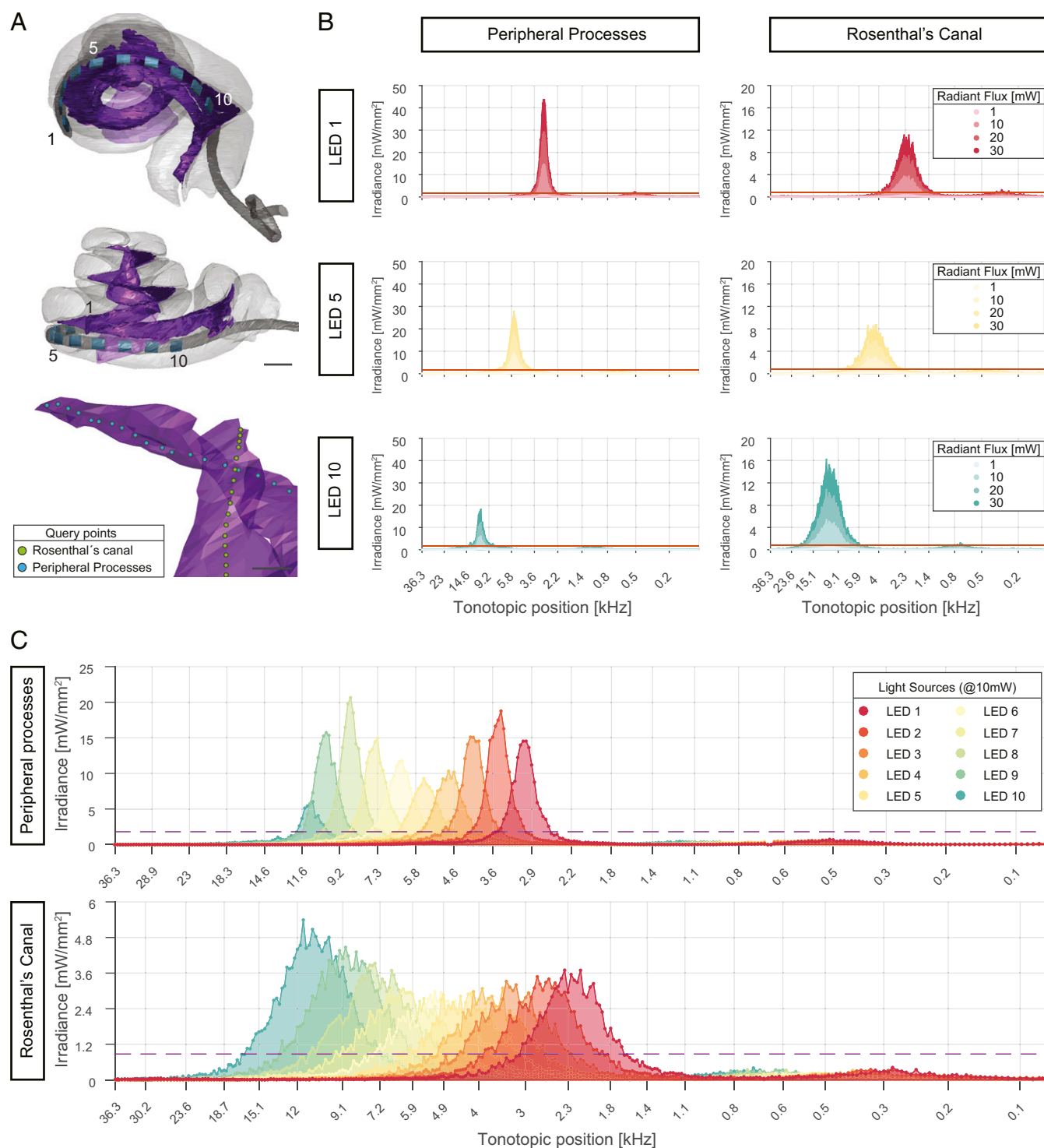
Keppeler et al.
Multiscale photonic imaging of the native and implanted cochlea
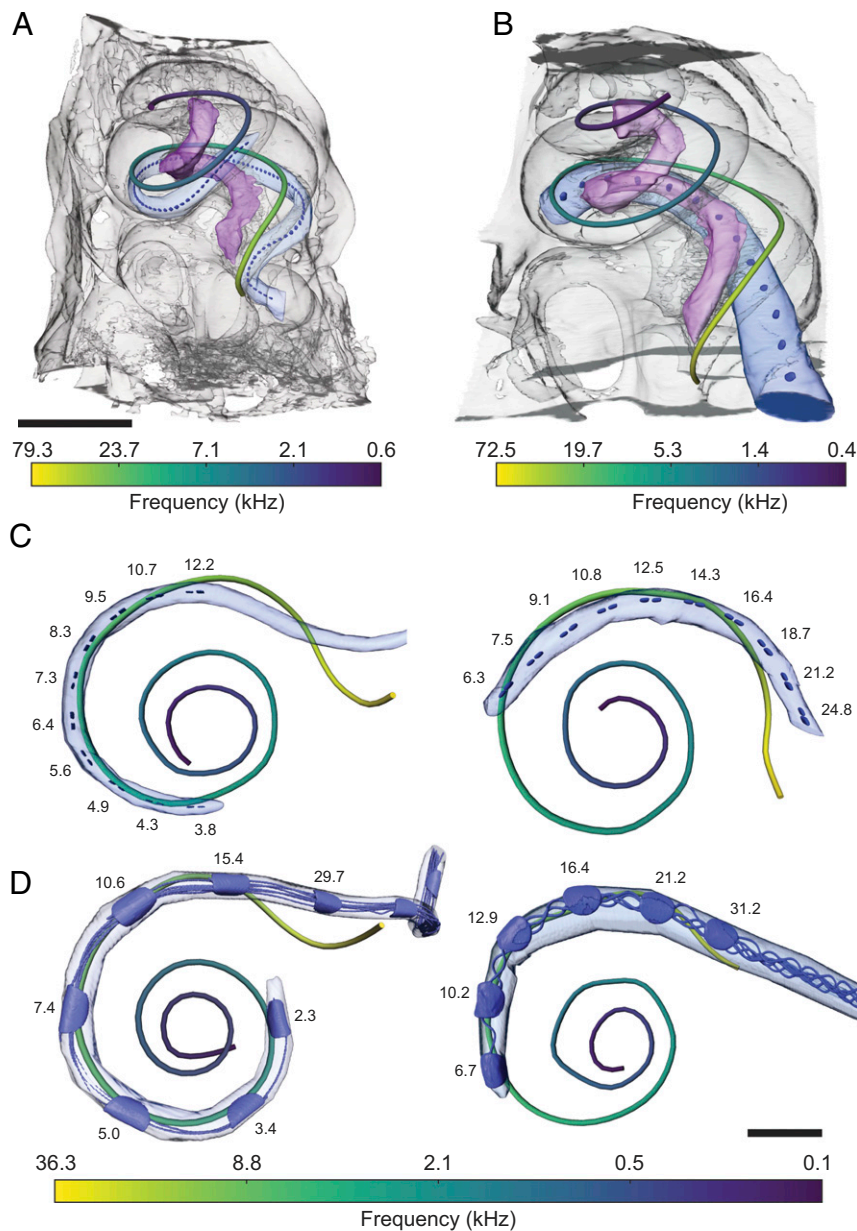
Fig. 5. Cochlear implantation studies in rodent and marmoset cochleae. (*A*) Mouse cochlea with an oCI comprising 93 μLEDs covering a frequency range from 72.2 to 2.5 kHz. Implantation was performed in fresh, explanted mouse cochleae that were chemically fixed thereafter. Insertion depth: 4.6 mm. Basilar membrane is color coded for corresponding frequency, Rosenthal's canal (purple), LED (blue), silicone (light blue), and bone (gray). View from lateral. (Scale bar, 1 mm.) (*B*) Rat cochlea with an oCI comprising 13 μLEDs covering a frequency range from 49.4 to 6.7 kHz. Implantation was performed in a fresh, explanted rat cochlea and chemically fixed subsequently. Insertion depth: 3.6 mm. View from lateral. Scale as in *A*. (*C*) oCI in marmoset scala tympani. Implantation was performed in fresh, postmortem marmoset skulls and chemically fixed subsequently. LED bond pads (blue), spacing between LEDs 300 μm, silicone (bright blue), and basilar membrane (color coded for corresponding frequency). View from cochlear base to apex. (*Left*) Best example, insertion depth: 7.6 mm. (*Right*) Insertion depth: 6.4 mm. Scale as in *D*. (*D*) Electrical CI in marmoset scala tympani. Implantation was performed in fresh marmoset skulls and chemically fixed subsequently. (*Left*) Best example, insertion depth: 8.9 mm; spacing: 1.5 mm. (*Right*) Insertion depth: 6 mm; spacing: 1 mm. (Scale bar, 1 mm.)

(47). Interestingly, like for the current study, this pioneering work of Spelman and colleagues was motivated by the necessity to quantify cochlear structure for the purpose of CIs (47). Next to X-ray–based imaging, such as microcomputed tomography, this volume imaging approach overcomes the challenges of reconstructions based on tissue sectioning—including compression and registration artifacts (48). Microcomputed tomography based on X-ray absorption contrast has been widely employed for nondestructive 3D structure determination of the cochlea (5, 25,

49–54). For small cochleae such as those of rodents, absorption by soft tissues is weak and harnessing sample-induced phase shifts in XPCT (55, 56) is well suited (53, 54, 57). Various X-ray sources have been employed successfully for XPCT: from laboratory sources (3, 5, 9, 53), to compact synchrotron (54), to third generation synchrotron (57). Using Fourier-based phase reconstruction, subcellular resolution (2 μm) can be achieved for the soft tissues even with laboratory sources, enabling, for example, the visualization of the thin Reissner's membrane (53). Here, XPCT using a laboratory source

Keppeler et al.
Multiscale photonic imaging of the native and implanted cochlea
www.manaraa.com

Fig. 6. Modeling optical stimulation in the marmoset cochlea. (*A*) Upper and middle panel show different views of reconstructed volumes from X-ray tomography (Fig. 5*C*) used in the simulations, depicting a marmoset cochlea with an inserted oCI. (Scale bar, 500 µm.) Lower close-up displaying the localization of query points in the apical turn. Purple: Rosenthal's canal and peripheral processes; light gray: scalae tympani, vestibuli, and media; blue: µLEDs of oCI, numbered 1 to 10 from apex; dark gray: flexible substrate of oCI. The centerline of Rosenthal's canal was used for query-point placement of the spiral ganglion. (Scale bar, 100 µm.) (*B*) Light irradiance profiles obtained from µLED 1, 5, and 10 at query points placed in Rosenthal's canal and the outermost edge of the peripheral processes. Orange line displays irradiance threshold values (1.81 mW/mm² for peripheral processes; 0.87 mW/mm² for Rosenthal's canal). (*C*) Light irradiance profiles from all light sources interrogated at a radiant flux of 10 mW indicate a spread of excitation of 0.91 to 1.19 octaves at Rosenthal's canal and 0.29 to 0.53 at peripheral processes for maximal stimulation amenable for these emitters. Dashed lines display irradiance threshold values (*SI Appendix*, Tables S2 and S3).

was used to obtain morphological parameters relevant for research on intracochlear drug administration and CI development for several animal models of auditory research. Moreover, synchrotron-based XPCT as well as LSFM were employed on the same samples and both enabled visualization of hair cells in the organ of Corti and SGNs in Rosenthal's canal. LSFM of the cochlea [e.g., ref. (58,

www.manaraa.com

59)]; with < 30 publications; for a review, see ref. 60), compared with applications in developmental biology (e.g., ref. 61) or imaging of the brain (e.g., ref. 62), seems to not have yet unfolded its full potential in those >25 y since the pioneering study (47). LSFM of the cochlea does not only provide structural information but, when combined with immunostaining, also offers molecular information. Here, we adapted the iDisco+ clearing protocol (39) for the cochlea (hence, nicknamed cDisco, reference *SI Appendix,* Fig. S1 for an overview of clearing approaches) that we found to work well in combination with immunofluorescence analysis. Next to the weeks required for cDisco, penetration of the primary and secondary antibodies make the tissue preparation time consuming (*SI Appendix,* Fig. S2), highlighting the immediate readiness as an advantage of X-ray tomography in case molecular information is dispensable. The overall time required for tissue preparation scaled with the extent of temporal bone: least for isolated mouse cochlea, longest for marmoset cochlea embedded in substantial temporal bone. The time for molecular labeling can be reduced when employing smaller probes, for example, such as nanobodies, either for direct immunolabeling or as secondary probes for premixing with the primary antibody (63). The analysis of the 3D light-sheet data enabled the approximation of the frequency-place map (Fig. 2E and *SI Appendix,* Table S5) and a proof of principle for automated counting of SGNs (Fig. 2F and *SI Appendix,* Figs. S3 and S4). Clearly, future studies aiming at counting of hair cells, SGNs, their molecular profiles, and/or assessing the rate of viral transduction, and the expression of exogenous proteins will need to further advance immunolabeling and resolve multicolor LSFM and data analysis. Moreover, it will be of interest to extend the method's utility for multiscale imaging to smaller (e.g., subcellular) structures such as the synapses in the organ of Corti.

Multimodal imaging, as performed in a sequential manner in the present study, offers access to additional information on the biological sample such as on cells of interest and their location relative to coordinates of the organ. Provided comparable fields of view and resolution, or potentially even multiscaling utility, as is the case for LSFM and X-ray tomography, this paves the way for comprehensive structural analysis.

Implications for Translational Studies. The morphological analysis by XPCT has instructed the design of oCIs for mice, rats, gerbils, and marmosets. For example, despite the small size of the mouse cochlea (roughly a fifth of the human cochlea), we managed to double the previously reported eCI insertion depth (*SI Appendix,* Table S4) when implanting a dedicated mouse µLED-based oCI (13, 14) (4.7 mm, covering 80% of the tonotopic axis). Likewise, in rats the thicker microfabricated oCIs based on larger, commercial LEDs (24) could reach a lower-frequency region (6.7 kHz) than known for eCIs from literature (*SI Appendix,* Table S4). Still, these oCIs could not be fully inserted, and future oCI studies in rats should consider the more suitable mold-encapsulation or µLED-based oCIs with smaller diameter and/or conical shape. The microfabricated oCIs were more compatible with implantation into the larger marmoset cochlea, where in the best case we achieved an insertion depth of ∼8 mm with a covered frequency-place range from 2.3 to 29.7 kHz. This matches previously reported insertion depth for eCIs (25) but exceeded the frequency coverage due to using round-window insertion in our study, gaining access to the high-frequency hook region of the cochlea as compared with cochleostomy in ref. 25. Using a newly developed marmoset 10-channel eCI electrode array, we achieved full insertion in three of four marmosets with an insertion depth of 12 mm reaching up to the low-frequency range (approximately up to 1 kHz), while we could position seven contacts with an insertion depth of ∼8 mm in another animal. Considering the near-linear decrease of scala tympani height from base to apex in all analyzed species, a conical probe design could further optimize the fit of the oCI, serve deeper insertion depth, and may help avoid damage to the sensitive scala

tympani (64, 65). Yet, considering the ellipsoid cross-section of scala tympani, a more complex probe design could benefit the implantation depth further.

We consider 10 channels sufficient for unfolding the full potential of the eCI in the marmoset, whose cochlea is about half of the human size, and the established 10-channel LED oCI can serve the comparative analysis of channel discrimination and frequency selectivity. Based on the reconstruction of the X-ray tomography of an oCI-implanted cochlea, we modeled light propagation from the 10 LEDs for a first assessment of the spectral selectivity of optogenetic stimulation of the marmoset cochlea. Assuming threshold irradiances observed in rodent experiments and simulating strong radiant fluxes (10 mW), the model predicts a maximal spread of excitation of ∼1 octave at the level of the spiral ganglion in Rosenthal's canal and of 0.4 octaves at the level of the peripheral SGN processes. While the irradiance profiles of neighboring LEDs show partial overlap for strong stimuli, we postulate that channel discrimination will be possible even with these large Lambertian emitters. Future studies using µLED-based or waveguide-based oCIs should establish dozens of optical stimulation channels in preparation of clinical translation in both rodents and marmosets and employ physiological and behavioral approaches to assess the frequency resolution of optogenetic hearing for blue-, and even more importantly, red-light stimulation. Red-light stimulation has the advantage of neural stimulation with less tissue scattering and lower risk of phototoxicity and, therefore, seems most suitable for future clinical optogenetic hearing restoration (66). Preclinical development of the oCI will benefit from post hoc multimodal imaging that will inform on the efficiency and safety of the gene therapy (e.g., AAV-mediated optogenetic manipulation of SGNs) and the safety of acute and chronic oCI stimulation (see review in ref. 66). Our study also proves the principle for automatic segmentation of cells in the 3D datasets acquired by LSFM and X-ray tomography, paving the way for future studies with efficient and comprehensive counting of neurons and/or hair cells as well as quantification of protein expression. Future LSFM experiments of the cleared and immunolabeled cochlea should aim at informing on the maintenance of peripheral SGN neurites and their synapses as well as on pathological changes of the cochlea—potentially resulting from immune responses, neurodegeneration, or phototoxicity. LSFM and X-ray microscopy complement each other (*SI Appendix,* Table S5) and can be performed on the same cochlea (Fig. 3). Such multimodal imaging supports the development of both the gene therapy and the medical device, for example, by analyzing SGN transduction, position of the oCI within the cochlea and the spatial relation of emitters and SGNs. As illustrated by our work on the large marmoset cochlea, LFSM should be applicable to the human cochlea provided sufficient time for decalcification and clearing is employed. Moreover, both methods will be helpful for evaluating the status of chronically implanted cochleae including the assessment of the foreign body response induced by the implant. Taken together, the multiscale, multimodal photonic imaging of the cochlea will facilitate preclinical studies of innovative approaches to deafness such as gene therapy and optogenetic CIs.

Materials and Methods

All experiments complied with national animal care guidelines and were approved by the Animal Welfare Office of the State of Lower Saxony. For details of animals, sample preparation, CIs, XPCT, LSFM, and data analysis, see *SI Appendix, Materials and Methods.*

Data Availability. Dataset data have been deposited in Göttingen Research Online / Data (GRO.data) (https://doi.org/10.25625/PDTX5K) (37). All other study data are included in the article and/or *SI Appendix.* Previously published data were used for this work (38).

1. A. Kral, R. Hartmann, D. Mortazavi, R. Klinke, Spatial resolution of cochlear implants: The electrical field and excitation of auditory afferents. *Hear. Res.* **121**, 11–28 (1998).

2. R. Kang *et al.*, Development and validation of the university of Washington clinical assessment of music perception test. *Ear Hear.* **30**, 411–418 (2009).

3. V. H. Hernandez *et al.*, Optogenetic stimulation of the auditory pathway. *J. Clin. Invest.* **124**, 1114–1129 (2014).

4. T. Mager *et al.*, High frequency neural spiking and auditory signaling by ultrafast red-shifted optogenetics. *Nat. Commun.* **9**, 1750 (2018).

5. C. Wrobel *et al.*, Optogenetic stimulation of cochlear neurons activates the auditory pathway and restores auditory-driven behavior in deaf adult gerbils. *Sci. Transl. Med.* **10**, eaao0540 (2018).

6. M. J. Duarte *et al.*, Ancestral adeno-associated virus vector delivery of opsins to spiral ganglion neurons: Implications for optogenetic cochlear implants. *Mol. Ther.* **26**, 1931–1939 (2018).

7. W. L. Hart *et al.*, Combined optogenetic and electrical stimulation of auditory neurons increases effective stimulation frequency-an in vitro study. *J. Neural Eng.* **17**, 016069 (2020).

8. D. Keppeler *et al.*, Ultrafast optogenetic stimulation of the auditory pathway by targeting-optimized Chronos. *EMBO J.* **37**, e99649 (2018).

9. A. Dieter, C. J. Duque-Afonso, V. Rankovic, M. Jeschke, T. Moser, Near physiological spectral selectivity of cochlear optogenetics. *Nat. Commun.* **10**, 1962 (2019).

10. A. Dieter *et al.*, μLED-based optical cochlear implants for spectrally selective activation of the auditory nerve. *EMBO Mol. Med.* **12**, e12387 (2020).

11. C.-P. Richter *et al.*, Spread of cochlear excitation during stimulation with pulsed infrared radiation: Inferior colliculus measurements. *J. Neural Eng.* **8**, 056006 (2011).

12. S. Ayub *et al.*, "High-density probe with integrated thin-film micro light emitting diodes (microLEDs) for optogenetic applications" in *IEEE 29th International Conference on Micro Electro Mechanical Systems (MEMS)*, D. Abbott, Ed. (IEEE, New York, 2016), pp. 379–382.

13. C. Goßler *et al.*, GaN-based micro-LED arrays on flexible substrates for optical cochlear implants. *J. Phys. Appl. Phys.* **47**, 205401 (2014).

14. E. Klein, C. Gossler, O. Paul, P. Ruther, High-density μLED-Based optical cochlear implant with improved thermomechanical behavior. *Front. Neurosci.* **12**, 659 (2018).

15. M. Schwaerzle *et al.*, "Led-based optical cochlear implant on highly flexible triple layer polyimide substrates" in *IEEE 29th International Conference on Micro Electro Mechanical Systems (MEMS)*, D. Abbott, Ed. (IEEE, New York, 2016), pp. 395–398.

16. Y. Xu *et al.*, Multichannel optrodes for photonic stimulation. *Neurophotonics* **5**, 045002 (2018).

17. S. Balster *et al.*, Optical cochlear implant: Evaluation of insertion forces of optical fibres in a cochlear model and of traumata in human temporal bones. *Biomed. Tech. (Berl.)* **59**, 19–28 (2014).

18. H. Zeng, L. Madisen, Mouse transgenic approaches in optogenetics. *Prog. Brain Res.* **196**, 193–213 (2012).

19. H. Tomita *et al.*, Visual properties of transgenic rats harboring the channelrhodopsin-2 gene regulated by the thy-1.2 promoter. *PLoS One* **4**, e7679 (2009).

20. I. B. Witten *et al.*, Recombinase-driver rat lines: Tools, techniques, and optogenetic application to dopamine-mediated reinforcement. *Neuron* **72**, 721–733 (2011).

21. S. Irving *et al.*, Cochlear implantation for chronic electrical stimulation in the mouse. *Hear. Res.* **306**, 37–45 (2013).

22. J. King, I. Shehu, J. T. Roland Jr, M. A. Svirsky, R. C. Froemke, A physiological and behavioral system for hearing restoration with cochlear implants. *J. Neurophysiol.* **116**, 844–858 (2016).

23. W. Lu, J. Xu, R. K. Shepherd, Cochlear implantation in rats: A new surgical approach. *Hear. Res.* **205**, 115–122 (2005).

24. D. Keppeler *et al.*, Multichannel optogenetic stimulation of the auditory pathway using microfabricated LED cochlear implants in rodents. *Sci. Transl. Med.* **12**, eabb8086 (2020).

25. L. A. Johnson, C. C. Della Santina, X. Wang, Temporal bone characterization and cochlear implant feasibility in the common marmoset (Callithrix jacchus). *Hear. Res.* **290**, 37–44 (2012).

26. M. S. Osmanski, X. Wang, Measurement of absolute auditory thresholds in the common marmoset (Callithrix jacchus). *Hear. Res.* **277**, 127–133 (2011).

27. X. Song, M. S. Osmanski, Y. Guo, X. Wang, Complex pitch perception mechanisms are shared by humans and a New World monkey. *Proc. Natl. Acad. Sci. U.S.A.* **113**, 781–786 (2016).

28. M. Busse *et al.*, Three-dimensional virtual histology enabled through cytoplasm-specific X-ray stain for microscopic and nanoscopic computed tomography. *Proc. Natl. Acad. Sci. U.S.A.* **115**, 2293–2298 (2018).

29. K. De Clercq *et al.*, High-resolution contrast-enhanced microCT reveals the true three-dimensional morphology of the murine placenta. *Proc. Natl. Acad. Sci. U.S.A.* **116**, 13927–13936 (2019).

30. H. Dejea *et al.*, Comprehensive analysis of animal models of cardiovascular disease using multiscale x-ray phase contrast tomography. *Sci. Rep.* **9**, 1–12 (2019).

31. M. Töpperwien, A. Markus, F. Alves, T. Salditt, Contrast enhancement for visualizing neuronal cytoarchitecture by propagation-based x-ray phase-contrast tomography. *Neuroimage* **199**, 70–80 (2019).

32. L. Massimi *et al.*, Exploring Alzheimer's disease mouse brain through X-ray phase contrast tomography: From the cell to the organ. *Neuroimage* **184**, 490–495 (2019).

33. A. Khimchenko *et al.*, Hard X-ray nanoholotomography: Large-scale, label-free, 3D neuroimaging beyond optical limit. *Adv. Sci. (Weinh.)* **5**, 1700694 (2018).

34. X. Mei *et al.*, Vascular supply of the human spiral ganglion: Novel three-dimensional analysis using synchrotron phase-contrast imaging and histology. *Sci. Rep.* **10**, 1–10 (2020).

35. W. Vågberg, J. Persson, L. Szekely, H. M. Hertz, Cellular-resolution 3D virtual histology of human coronary arteries using x-ray phase tomography. *Sci. Rep.* **8**, 11014 (2018).

36. M. Töpperwien, F. van der Meer, C. Stadelmann, T. Salditt, Three-dimensional virtual histology of human cerebellum by X-ray phase-contrast tomography. *Proc. Natl. Acad. Sci. U.S.A.* **115**, 6940–6945 (2018).

37. Daniel Keppeler *et al.*, Supplementary data for: Multiscale photonic imaging of the native and implanted cochlea. Göttingen Research Online / Data. https://doi.org/10.25625/PDTX5K. Deposited 10 April 2021.

38. Mauricio Reyes, Medical Dataset: Raw Image (CT) of Cochlea from subject of age XXSMIR.Cochlea.XX.O.CT.29498.000.dcm. *SICAS Medical Image Repository*, https://doi.org/10.22016/SMIR.O.29498 (2014).

39. N. Renier *et al.*, iDISCO: A simple, rapid method to immunolabel large tissue samples for volume imaging. *Cell* **159**, 896–910 (2014).

40. D. D. Greenwood, A cochlear frequency-position function for several species–29 years later. *J. Acoust. Soc. Am.* **87**, 2592–2605 (1990).

41. C. J. D, Afonso, "Development and application of tools for the characterization of the optogenetics stimulation of the cochlea type," PhD thesis, Georg-August-Universität Göttingen, Göttingen, Germany (2020).

42. M. Thorne *et al.*, Cochlear fluid space dimensions for six species derived from reconstructions of three-dimensional magnetic resonance images. *Laryngoscope* **109**, 1661–1668 (1999).

43. J. Lee, J. B. Nadol Jr, D. K. Eddington, Depth of electrode insertion and postoperative performance in humans with cochlear implants: A histopathologic study. *Audiol. Neurotol.* **15**, 323–331 (2010).

44. A. Laubsch, M. Sabathil, J. Baur, M. Peter, B. Hahn, High-power and high-efficiency InGaN-based light emitters. *IEEE Trans. Electron Dev.* **57**, 79–87 (2010).

45. M. Müller, K. von Hünerbein, S. Hoidis, J. W. T. Smolders, A physiological place-frequency map of the cochlea in the CBA/J mouse. *Hear. Res.* **202**, 63–73 (2005).

46. H. Siedentopf, R. Zsigmondy, Uber Sichtbarmachung und Größenbestimmung ultramikoskopischer Teilchen, mit besonderer Anwendung auf Goldrubingläser. *Ann. Phys.* **315**, 1–39 (1902).

47. A. H. Voie, D. H. Burns, F. A. Spelman, Orthogonal-plane fluorescence optical sectioning: Three-dimensional imaging of macroscopic biological specimens. *J. Microsc.* **170**, 229–236 (1993).

48. J. A. Buytaert, S. B. Johnson, M. Dierick, W. H. Salih, P. A. Santi, MicroCT versus sTSLIM 3D imaging of the mouse cochlea. *J. Histochem. Cytochem.* **61**, 382–395 (2013).

49. T. Shibata, T. Nagano, Applying very high resolution microfocus X-ray CT and 3-D reconstruction to the human auditory apparatus. *Nat. Med.* **2**, 933–935 (1996).

50. U. Vogel, New approach for 3D imaging and geometry modeling of the human inner ear. *ORL J. Otorhinolaryngol. Relat. Spec.* **61**, 259–267 (1999).

51. R. Glueckert *et al.*, Histology and synchrotron radiation-based microtomography of the inner ear in a molecularly confirmed case of CHARGE syndrome. *Am. J. Med. Genet. A.* **152A**, 665–673 (2010).

52. C.-F. Lee *et al.*, Registration of micro-computed tomography and histological images of the Guinea pig cochlea to construct an ear model using an iterative closest point algorithm. *Ann. Biomed. Eng.* **38**, 1719–1727 (2010).

53. M. Bartels, V. H. Hernandez, M. Krenkel, T. Moser, T. Salditt, Phase contrast tomography of the mouse cochlea at microfocus x-ray sources. *Appl. Phys. Lett.* **103**, 083703 (2013).

54. M. Töpperwien *et al.*, Propagation-based phase-contrast x-ray tomography of cochlea using a compact synchrotron source. *Sci. Rep.* **8**, 4922 (2018).

55. P. Cloetens *et al.*, Holotomography: Quantitative phase tomography with micrometer resolution using hard synchrotron radiation x rays. *Appl. Phys. Lett.* **75**, 2912–2914 (1999).

56. S. Mayo *et al.*, X-ray phase-contrast microscopy and microtomography. *Opt. Express* **11**, 2289–2302 (2003).

57. C. Rau, I. K. Robinson, C.-P. Richter, Visualizing soft tissue in the mammalian cochlea with coherent hard X-rays. *Microsc. Res. Tech.* **69**, 660–665 (2006).

58. K. M. Brody *et al.*, A new method for three-dimensional immunofluorescence study of the cochlea. *Hearing Research*, 10.1016/j.heares.2020.107956 (2020).

59. K. A. Hutson *et al.*, Light sheet microscopy of the gerbil cochlea. *J Comp Neurol* **529**, 757–785 (2021).

60. P. A. Santi, Light sheet fluorescence microscopy: A review. *J. Histochem. Cytochem.* **59**, 129–138 (2011).

61. J. Huisken, J. Swoger, F. Del Bene, J. Wittbrodt, E. H. K. Stelzer, Optical sectioning deep inside live embryos by selective plane illumination microscopy. *Science* **305**, 1007–1009 (2004).

62. H.-U. Dodt *et al.*, Ultramicroscopy: Three-dimensional visualization of neuronal networks in the whole mouse brain. *Nat. Methods* **4**, 331–336 (2007).

63. S. Sograte-Idrissi *et al.*, Circumvention of common labelling artefacts using secondary nanobodies. *Nanoscale* **12**, 10226–10239 (2020).

64. F.-G. Zeng, S. Rebscher, W. Harrison, X. Sun, H. Feng, Cochlear implants: System design, integration, and evaluation. *IEEE Rev. Biomed. Eng.* **1**, 115–142 (2008).

65. S. J. Rebscher *et al.*, Considerations for design of future cochlear implant electrode arrays: Electrode array stiffness, size, and depth of insertion. *J. Rehabil. Res. Dev.* **45**, 731–747 (2008).

66. S. Kleinlogel, C. Vogl, M. Jeschke, J. Neef, T. Moser, Emerging approaches for restoration of hearing and vision. *Physiol. Rev.* **100**, 1467–1525 (2020).

NEUROSCIENCE

Keppeler et al.
Multiscale photonic imaging of the native and implanted cochlea

www.manaraa.com